

Full length article

# Controlled formation of coherent cuboidal nanoprecipitates in body-centered cubic high-entropy alloys based on $\text{Al}_2(\text{Ni}, \text{Co}, \text{Fe}, \text{Cr})_{14}$ compositions

Y. Ma<sup>a</sup>, Q. Wang<sup>a,\*</sup>, B.B. Jiang<sup>a</sup>, C.L. Li<sup>a</sup>, J.M. Hao<sup>a</sup>, X.N. Li<sup>a</sup>, C. Dong<sup>a</sup>, T.G. Nieh<sup>b,\*\*</sup>

<sup>a</sup> Key Laboratory of Materials Modification By Laser, Ion and Electron Beams (Ministry of Education), School of Materials Science and Engineering, Dalian University of Technology, Dalian 116024, China

<sup>b</sup> Department of Materials Science and Engineering, University of Tennessee, Knoxville, TN 37996, USA

## ARTICLE INFO

### Article history:

Received 3 October 2017  
 Received in revised form  
 2 January 2018  
 Accepted 5 January 2018  
 Available online 3 February 2018

### Keywords:

High entropy alloys  
 Coherent precipitation  
 Lattice misfit  
 Microstructural evolution  
 Precipitation strengthening

## ABSTRACT

Microstructures and mechanical properties of Al-Ni-Co-Fe-Cr high-entropy alloys (HEAs) were investigated by systematically varying transition metals instead of Al, within the chemical formula of  $\text{Al}_2\text{M}_{14}$  (M represents different mutations of transition metals). The formation of different crystal structures (FCC, BCC, or FCC+BCC mixture) and its effects on the resulting mechanical properties of this series of HEAs, both in tension and compression, were evaluated. It was found that, in the BCC-dominated HEAs, ordered B2 precipitates were always coherently dispersed in the BCC solid-solution matrix. The shape of these B2 precipitates was strongly affected by the lattice misfit between the disordered BCC and ordered B2. A uniform distribution of cuboidal B2 particles could be obtained by properly adjusting M, thus the lattice misfit, in a manner similar to that in Ni-based superalloys. Strengthening effects caused by different BCC/B2 morphologies were also estimated and compared with experimental measurements. The optimal strengthening as a function of the shape and size of the coherent precipitates was discussed in light of the lattice misfit in these HEAs.

© 2018 Acta Materialia Inc. Published by Elsevier Ltd. All rights reserved.

## 1. Introduction

The development of new types of metallic materials always draws large attention from materials community because of the potential of engineering applications. Traditional design of structural alloys is to select the principal element based on a specific property requirement, and further to use alloying additions to confer secondary properties without sacrificing the primary property. Such design concept has led to the development of many advanced alloys and, over the past few decades, significant knowledge and theories about alloys based on one principal component have been accumulated. Recently, a new class of compositionally complex alloys, namely, high-entropy alloys (HEAs) or multi-principal elements alloys (MPEAs), has developed and these alloys exhibited many unique properties, for example, high strength/ductility and good fracture toughness [1–6].

Different from the traditional alloys, HEAs generally contain multiple principal elements (>5) in equimolar or near-equimolar proportions and often have a simple crystal structure, e.g., face-centered cubic (FCC), body-centered cubic (BCC), hexagonal close-packed (HCP) solid solutions, or their ordered derivatives (such as  $cP4\text{-AuCu}_3$  (L1<sub>2</sub>) and  $cP2\text{-CsCl}$  (B2)) [5–8]. Interestingly, common strengthening mechanisms found in traditional alloys, such as solid solution strengthening [9], precipitation strengthening [10,11], dislocation and grain boundary strengthening [12], as well as TWIP (twinning-induced plasticity) and TRIP (transformation-induced plasticity) effects [13,14], have all been reported to occur in HEAs.

Based on the constituent elements, HEAs can be classified into three types: late transition metals (LTMs, e.g., Mn, Fe, Co, Ni, Cu)-based FCC HEAs [12–21], early transition metals (ETMs, e.g., Ti, V, Mo, W)-based BCC refractory high-entropy alloys (RHEAs) [22–26], and Al-TMs HEAs (including mixed ETMs and LTMs) with dual-phase structures (FCC+BCC) [27–36]. A large variety of crystal phases and microstructures render HEAs with diverse properties, especially mechanical properties. For example, an FCC single-phase CoCrFeMnNi HEA (also known as Cantor Alloy), as a result of easy twinning in the material, exhibited a higher work hardening

\* Corresponding author.

\*\* Corresponding author.

E-mail addresses: [wangq@dlut.edu.cn](mailto:wangq@dlut.edu.cn) (Q. Wang), [tnieh@utk.edu](mailto:tnieh@utk.edu) (T.G. Nieh).

capability and improved ductility than all the traditional alloys at cryogenic temperatures [15]. Some metastable HEAs with a non-equimolar mixing of elements also showed prominent mechanical properties induced by either TWIP or TRIP effect [13,14]. The highest strength has been reported in BCC-based RHEAs, such as CrNbTiVZr [22]. In the case of Al-LTM HEAs, in particular, the mechanical properties appeared to be tunable because of their microstructural diversities. An  $\text{Al}_{0.5}\text{NiCoFeCrCu}$  HEA [30], which has a dual-phase FCC/BCC structure, exhibited a higher tensile strength than the single-phase FCC ( $\text{Al}_x\text{NiCoFeCr}$ ) HEAs with the Al content less than 0.3 [32–35].

For material strengthening, it has been demonstrated that, through alloying, coherent spherical  $\text{L}_{12}\text{-Ni}_3(\text{Al}, \text{Ti})$  particles were produced in an FCC ( $\text{FeCoNiCr}$ ) $_{94}\text{Ti}_2\text{Al}_4$  HEA (in atomic percent, at. %) which led to a significant strength improvement [10]. This result is intriguing since precipitation hardening is well known to occur in traditional Ni-based and Co-based superalloys with  $\gamma\text{-FCC}/\gamma'\text{-L}_{12}$  microstructures [37–39], in which the mechanism actually dominates the high-temperature performance. However, despite of the fact that precipitation strengthening has been widely reported in FCC-based alloys, the mechanism appears to occur much less often in BCC-based alloys. Coherent nanoprecipitation has not yet been developed to enhance ultra-high strength ferritic steels [40,41]. It was fascinating to note that, in a recent study of a BCC lightweight  $\text{AlM}_{0.5}\text{NbTa}_{0.5}\text{TiZr}$  HEA, cuboidal BCC particles were observed to coherently embed in the B2 matrix, besides some plate-like BCC precipitates [27]. In addition, alloying Al to FCC-HEAs has been recognized and frequently used to shift the structure from FCC to BCC for the strength improvement [31–35]. However, in the high Al-containing BCC HEAs, the B2 and BCC phases often form a weave-like microstructure, as a result of spinodal decomposition [31–35]. Consequently, the plasticity of these BCC HEAs is severely deteriorated, for example, the high-strength  $\text{AlNiCoFeCr}$  has virtually no tensile ductility [31]. It is challenging, but highly desirable, to produce microstructures with a uniform distribution of ordered B2 particles in disordered BCC alloy matrix.

Whereas adjusting the Al content is frequently used to alter the microstructures of Al-TM HEAs [32–35], there was limited or no effort to study the role of transition metals. Therefore, in this study, we aim at investigating the microstructural evolution and the corresponding mechanical properties of the Al-Ni-Co-Fe-Cr (Al-TM) alloy system by mutating the transition metals, instead of varying the Al content. The HEAs used for this study are designed based on the cluster formula approach we recently developed [42,43]. The shape and size of the coherently-precipitated BCC or B2 particles formed in these HEAs will be discussed in light of lattice misfit. Strength improvement caused by the presence of coherent B2 precipitates in BCC-dominant alloys will be analyzed and the stability of these precipitates at high temperatures will also be addressed.

## 2. Composition design of Al-Ni-Co-Fe-Cr HEAs based on the cluster formula approach

The cluster formula approach [42,43] used for the design of alloy compositions was based on the chemical short-range orders (CSROs) in solid solutions proposed initially by Cowley [44] and Friedel [45]. The stronger CSROs (denoted as the nearest-neighbor clusters centered by a solute atom having strong interaction with the base solvent atoms) are interconnected by additional atoms (i.e. glue atoms with weak interactions) to form dense-packed 3D structure. In essence, this cluster approach visualizes CSROs in a solid solution as a local structural unit consisting of a nearest-neighbor cluster surrounded by several glue atoms. Consequently, a composition formula of  $[\text{cluster}](\text{glues})_m$  can be obtained, in

which the nearest-neighbor clusters are cuboctahedron with a coordination number of 12 (CN12) and a rhombi-dodecahedron with CN14 in FCC and BCC solid solutions, respectively [42,43]. Since HEAs can be treated as a special kind of solid solution alloys, CSROs have been confirmed in some HEAs by both neutron scattering experiments and simulations [46–48]. Thus, it is conceivable that the cluster formula approach can also conveniently extend to HEAs; in fact, the cluster model was recently validated in HEAs by neutron experiments [49].

In Al-TM HEA systems, Al interacts strongly with transition metals, while TMs are expected to exhibit only weak mutual interactions, as indicated by the enthalpies of mixing  $\Delta H$  [50]. For Al-Ni-Co-Fe-Cr, the enthalpies of mixing between Al-TM are  $\Delta H_{\text{Al-Ni}} = -22 \text{ kJ mol}^{-1}$ ,  $\Delta H_{\text{Al-Co}} = -19 \text{ kJ mol}^{-1}$ ,  $\Delta H_{\text{Al-Fe}} = -11 \text{ kJ mol}^{-1}$ , and  $\Delta H_{\text{Al-Cr}} = -10 \text{ kJ mol}^{-1}$ , much higher than those between TMs (enthalpies of mixing are nearly to zero [50]). Consequently, when applying the cluster formula approach to this system, all the TMs can be simply treated as a single virtual element M of the base solvent and Al serves as the solute element. Thus, the  $\text{Al}_x\text{NiCoFeCr}$  HEA series can be simply expressed by the pseudo-binary  $\text{Al}_x\text{M}_4$ , where  $\text{M} = \text{Ni}_1\text{Co}_1\text{Fe}_1\text{Cr}_1$  is the equimolar mixing of TMs. Following this notion, the alloy composition of  $\text{Al}_2\text{M}_{14}$  ( $\text{Al}_{12.5}\text{M}_{87.5}$ , at. %), derived from the cluster formula for either the FCC ( $[\text{Al-M}_{12}](\text{M}_2\text{Al}_1)$ ) or BCC ( $[\text{Al-M}_{14}]\text{Al}_1$ ) structures, is actually close to the upper limit of the Al-content (i.e.,  $\text{Al}_{11.1}\text{M}_{88.9}$  or  $\text{Al}_{0.5}\text{M}_4$ ) reported in the single-phase FCC- $\text{Al}_x\text{NiCoFeCr}$  alloys [32]. The crystal structures of  $\text{Al}_2\text{M}_{14}$  HEAs might be varied through changing the proportion of M from an equimolar mixing of TMs to a non-equimolar mixing, since all these TMs are different FCC- or BCC-stabilized elements.

Therefore, in the present work a series of new Al-Ni-Co-Fe-Cr HEAs are designed and synthesized based on the composition formula  $\text{Al}_2\text{M}_{14}$ , in which Al is fixed and M represents different mutations of the four transition metals. These alloys are specifically denoted as  $\text{M}_{1111} = \text{Ni}_1\text{Co}_1\text{Fe}_1\text{Cr}_1$  (No.1 alloy in Table 1),  $\text{M}_{4433} = \text{Ni}_4\text{Co}_4\text{Fe}_3\text{Cr}_3$  (No.2),  $\text{M}_{1121} = \text{Ni}_1\text{Co}_1\text{Fe}_2\text{Cr}_1$  (No.3), and  $\text{M}_{1112} = \text{Ni}_1\text{Co}_1\text{Fe}_1\text{Cr}_2$  (No.4). To evaluate the effect of Al addition, another alloy with a higher Al content, specifically,  $\text{Al}_3\text{M}_{14}$  ( $\text{M} = \text{Ni}_1\text{Co}_1\text{Fe}_1\text{Cr}_1$ ) (No.5) was also synthesized and studied. These alloys and their specific chemical compositions (at. %) are summarized in Table 1.

## 3. Experimental

Alloys used in this study were prepared by means of arc melting and suction cast into a 6 mm-diameter cylindrical copper mold under an argon atmosphere. Purities of the raw elemental metals are 99.99% for Al, Co, Fe, and Ni, and 99.9% for Cr, respectively. Mixtures of raw materials with appropriate compositions and a total weight of about 15 g were remelted at least four times to ensure chemical homogeneity before suction-casting. In order to investigate the microstructural stability of coherent precipitates at high temperatures, No.4 alloy samples ( $\text{M}_{1112} = \text{Ni}_1\text{Co}_1\text{Fe}_1\text{Cr}_2$ ) with a size of  $\phi 6 \times 8 \text{ mm}$  were additionally heat-treated at temperatures of 673, 873, 973, and 1073 K for 2 h and, then, followed by water-quenching.

Crystalline phases in these as-cast alloys were identified using a Bruker D8 X-ray diffractometer (XRD) with the  $\text{Cu-K}_\alpha$  radiation ( $\lambda = 0.15406 \text{ nm}$ ), in which the external standard method was applied to calculate the lattice constants [51]. The microstructure was examined using either Olympus optical microscopy (OM), Zeiss Supra 55 scanning electron microscopy (SEM) with an energy dispersive spectrometer (EDS), Philips Tecnai  $\text{G}^2$  transmission electron microscopy (TEM) equipped with a selected-area electron diffraction (SAED) analysis, or Tecnai F30 scanning transmission electron microscopy (STEM). The etching solution used for sample

**Table 1**

Data summary for  $\text{Al}_2\text{M}_{14}$  and  $\text{Al}_3\text{M}_{14}$  alloy systems, including chemical composition, valence electron concentration (VEC), microhardness (HV), compressive yield strength  $\sigma_y^c$ , tensile yield strength  $\sigma_y^t$ , tensile ultimate strength  $\sigma_{UTS}^t$ , uniform elongation  $\delta$ , phase constitutions and their volume fraction.

No.	M	Chemical compositions (at. %)	VEC	HV	$\sigma_y^c$ (MPa)	$\sigma_y^t$ (MPa)	$\sigma_{UTS}^t$ (MPa)	$\delta$ (%)	Phase constitution + Volume fraction (%)
1	$\text{Al}_2(\text{NiCoFeCr})_{14}$ ( $\text{M}_{1111}$ )	$\text{Al}_{12.5}\text{Ni}_{21.875}\text{Co}_{21.875}\text{Fe}_{21.875}\text{Cr}_{21.875}$	7.59	285	614	598	930	15.6	FCC matrix + BCC/B2 (~35%)
2	$\text{Al}_2(\text{Ni}_4\text{Co}_4\text{Fe}_3\text{Cr}_3)_{14}$ ( $\text{M}_{4433}$ )	$\text{Al}_{12.5}\text{Ni}_{25}\text{Co}_{25}\text{Fe}_{18.75}\text{Cr}_{18.75}$	7.75	205	387	346	>728	>33.0	FCC matrix + BCC/B2 (~15%)
3	$\text{Al}_2(\text{NiCoFe}_2\text{Cr})_{14}$ ( $\text{M}_{1121}$ )	$\text{Al}_{12.5}\text{Ni}_{17.5}\text{Co}_{17.5}\text{Fe}_{35}\text{Cr}_{17.5}$	7.55	485	1085	991	1245	8.2	BCC/B2 matrix + FCC (~25%)
4	$\text{Al}_2(\text{NiCoFeCr}_2)_{14}$ ( $\text{M}_{1112}$ )	$\text{Al}_{12.5}\text{Ni}_{17.5}\text{Co}_{17.5}\text{Fe}_{17.5}\text{Cr}_{35}$	7.20	626	1718	–	–	–	BCC/B2
5	$\text{Al}_3(\text{NiCoFeCr})_{14}$ ( $\text{Al}_3\text{M}_{14}$ )	$\text{Al}_{17.64}\text{Ni}_{20.59}\text{Co}_{20.59}\text{Fe}_{20.59}\text{Cr}_{20.59}$	7.32	531	1399	–	–	–	BCC/B2

preparation for optical microscopy (OM) and SEM observations contains 5 g  $\text{FeCl}_3 \cdot 6\text{H}_2\text{O}$  + 25 ml HCl + 25 ml  $\text{C}_2\text{H}_5\text{OH}$ , and the TEM samples were prepared by twin-jet electro-polishing in a solution of 10%  $\text{HClO}_4$  + 90%  $\text{C}_2\text{H}_5\text{OH}$  (volume fraction) at a cryogenic temperature of 243 K. Statistical analysis on the volume fraction of FCC and BCC/B2 phases were performed with at least 6 OM images, and those on the particle size as well as volume fraction of precipitates in BCC/B2 regions were performed with at least 6 SEM or TEM morphology images.

For mechanical evaluation, both uniaxial compressive and tensile tests were conducted on an 810 Material Test System (MTS) at a nominal strain rate of  $2 \times 10^{-4}$ /s at room temperature. Cylindrical samples for compression have a size of  $\phi 3 \times 6$  mm were machined directly from the  $\phi 6$  mm cast rods. The rod-shaped tensile samples have a gauge dimension of 3 mm in diameter and 25 mm in length. For tensile tests, an extensometer was used to measure directly the deformation strain. For compression, the machine stiffness was first determined in order to compensate the deformation from test frame to get the real strain. It was measured by compressing a large-size (15 mm in diameter) 310S stainless steel sample with a known Young's modulus of 205 GPa, from which the force-displacement curve was obtained and machine stiffness was deduced after subtracting the elastic contribution from the 310S sample. The measured machine stiffness was subsequently integrated in the compressive strain to properly convert engineering compression to true compression. Two WC spacers were inserted between the compression platform and the test samples (top and bottom) during compression. At least three specimens of each alloy were tested, both tension and compression, under each condition. The fractography of several representative HEAs after tension was also examined using SEM. Values of microhardness of HEAs were measured using a HVS-1000 Vickers hardness tester under a constant load of 500 g for 20 s and at least 15 indents were taken.

## 4. Results

### 4.1. Microstructural characteristics

XRD patterns obtained from the as-cast alloys are shown in Fig. 1. The baseline alloy  $\text{M}_{1111}$  (No.1) consists of a dual-phase structure with the primary FCC plus 35% of BCC phase. With an addition of the FCC-stabilizers such as Ni and Co (both with a close-packed structure), diffraction peaks from BCC phase is suppressed, but the FCC phase is enhanced, for example, in  $\text{M}_{4433}$  alloy (No.2). This morphological change is also confirmed by the OM observation, as shown in Fig. 2a and b. In Fig. 2a, the alloy matrix of  $\text{M}_{1111}$  contains mainly bright FCC dendrites with dark BCC phase sandwiched between these dendrites, and the volume fraction of the BCC phase is estimated to be about 35%. In comparison, the amount

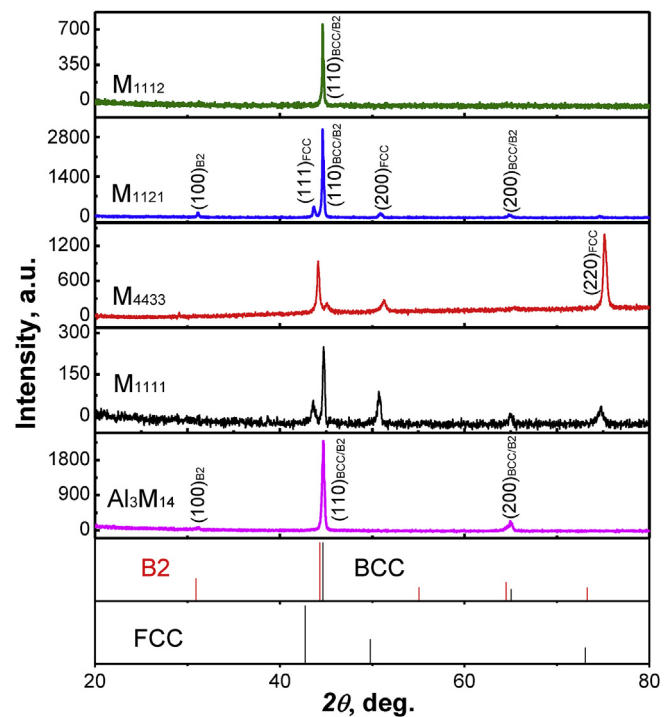


**Fig. 1.** XRD patterns from the as-cast  $\text{Al}_2\text{M}_{14}$  and  $\text{Al}_3\text{M}_{14}$  HEAs, in which M represents different mutations of transition metals of Ni, Co, Fe and Cr.

of BCC phase in  $\text{M}_{4433}$  is significantly reduced to only about 15% (Fig. 2b).

By contrast, when BCC-stabilizers such as Fe or Cr (with non-close-packed structure) is added to  $\text{M}_{1111}$ , the alloy structure tends to shift from FCC to BCC, as revealed by both the XRD and OM/SEM results. For instance, the microstructure of additional Fe-containing  $\text{M}_{1121}$  alloy (No.3) consists of coarse columnar BCC dendrites with 25% of FCC phase distributed within the interdendritic regions (Fig. 2c). In fact, when excessive strong BCC-stabilizer Cr is added ( $\text{M}_{1112}$ ), the structure becomes entirely BCC without any FCC phase (Fig. 2d). Therefore, by adjusting the combinations of TMs without the equimolar restriction, it is possible to alter the phase constitutions as well as the morphologies in the  $\text{Al}_2\text{M}_{14}$  alloy system, in a fashion similar to that to vary only the Al content. It is particularly pointed out that, the currently studied  $\text{Al}_3\text{M}_{14}$  alloy (No.5), which contains a higher Al, also exhibits a single BCC structure with columnar dendrites (Fig. 2e), quite similar to  $\text{M}_{1112}$ . The phase constitutions and their volume fractions in these HEAs are listed in Table 1. The chemical compositions and

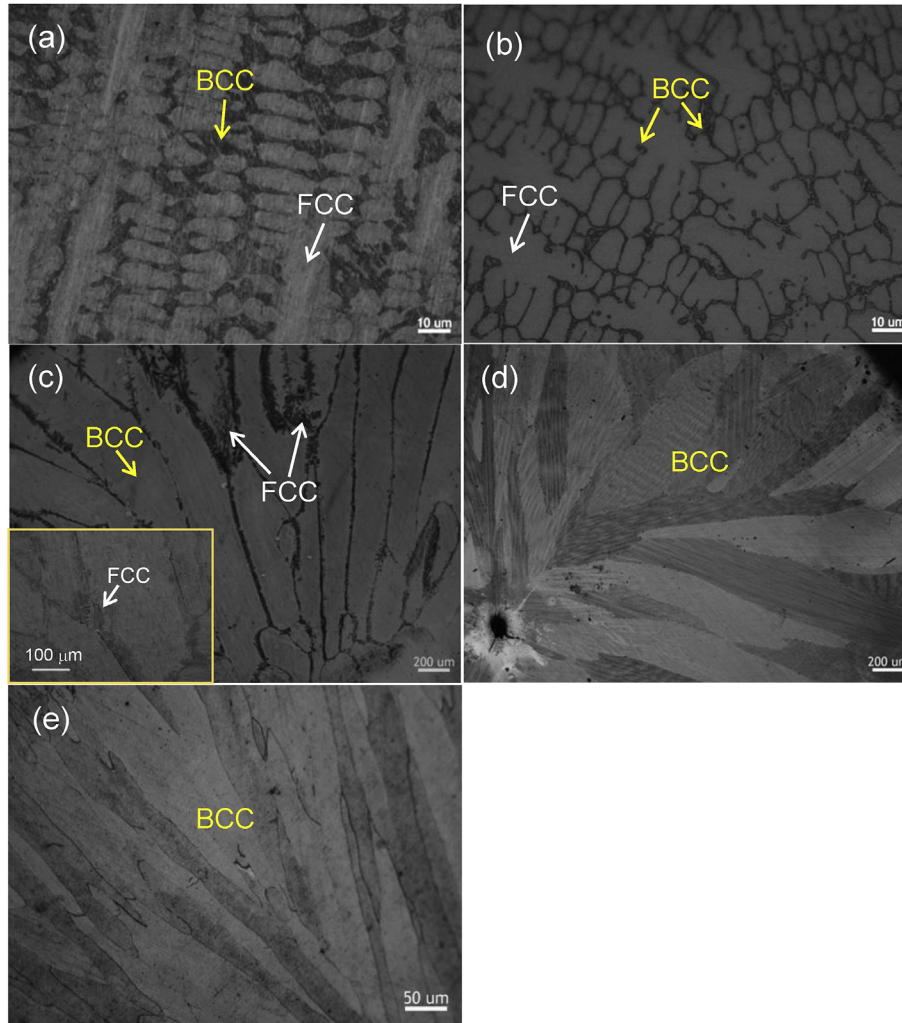


**Fig. 2.** OM micrographs of the as-cast  $\text{Al}_2\text{M}_{14}$  HEAs, (a)  $\text{M}_{1111}$ , (b)  $\text{M}_{4433}$ , (c)  $\text{M}_{1121}$ , and (d)  $\text{M}_{1112}$ ; and  $\text{Al}_3\text{M}_{14}$  HEA (e).

phases in different regions in these as-cast samples were measured by SEM-EDS and listed in Table 2. The measured compositions of the as-cast HEAs are noted to be quite close to their nominal values. Also, Al and Ni appear to distribute preferentially in the BCC/B2 regions, whereas Co and Fe appear to enter into the FCC regions.

To further reveal the microstructure of these samples in details, we selected three representative HEAs, specifically, FCC-dominated  $\text{M}_{4433}$ , and BCC-dominated  $\text{M}_{1121}$  and  $\text{M}_{1112}$ , for comparison. In the

FCC-dominated alloy  $\text{M}_{4433}$ , in addition to the major FCC dendritic matrix (Fig. 3a), the inter-dendritic region is composed of a composite morphology of ellipsoidal BCC nanoparticles (about 30–60 nm in dimension) dispersed in a B2 matrix, as shown in Fig. 3b. These BCC nanoparticles are actually coherent with the ordered B2 matrix, as indicated by the selected-area electron diffraction (SAED) pattern in the inset of Fig. 3b. Such a B2/BCC morphology has not yet been reported in Al-TM based HEAs with a

**Table 2**

Chemical compositions (at. %) in different regions or phases in the designed  $\text{Al}_2\text{M}_{14}$  and  $\text{Al}_3\text{M}_{14}$  HEAs measured by EDS. The variations for the EDS results are represented by the standard deviation from the measured series.

Alloys	Regions <sup>a</sup>	Crystal Structure	Al	Ni	Co	Fe	Cr
$\text{M}_{1111}$	O		$13.0 \pm 0.6$	$21.7 \pm 0.8$	$22.4 \pm 0.7$	$21.4 \pm 0.7$	$21.5 \pm 0.9$
	DR	FCC	$9.4 \pm 0.7$	$21.4 \pm 1.1$	$23.5 \pm 1.0$	$24.5 \pm 0.9$	$21.2 \pm 1.0$
	ID	BCC/B2	$13.4 \pm 0.7$	$22.6 \pm 0.9$	$21.4 \pm 0.9$	$21.0 \pm 0.8$	$21.6 \pm 0.9$
$\text{M}_{4433}$	O		$12.7 \pm 0.7$	$23.9 \pm 1.1$	$25.6 \pm 1.0$	$19.3 \pm 0.8$	$18.5 \pm 0.7$
	DR	FCC	$9.2 \pm 0.6$	$25.4 \pm 1.0$	$26.5 \pm 0.9$	$20.4 \pm 0.7$	$18.5 \pm 0.8$
	ID	BCC/B2	$21.2 \pm 0.9$	$29.9 \pm 1.0$	$21.1 \pm 0.9$	$13.8 \pm 0.6$	$14.0 \pm 0.7$
$\text{M}_{1121}$	O		$13.9 \pm 0.6$	$17.6 \pm 0.8$	$17.1 \pm 1.0$	$33.5 \pm 1.2$	$17.9 \pm 0.8$
	DR	BCC/B2	$14.5 \pm 0.8$	$17.0 \pm 1.0$	$16.6 \pm 0.9$	$33.7 \pm 1.3$	$18.2 \pm 0.8$
	ID	FCC	$12.5 \pm 0.5$	$17.4 \pm 0.8$	$17.5 \pm 0.7$	$35.2 \pm 1.1$	$17.4 \pm 0.6$
$\text{M}_{1112}$	O	BCC/B2	$13.0 \pm 0.6$	$17.1 \pm 0.7$	$17.7 \pm 0.7$	$17.2 \pm 0.6$	$35.0 \pm 1.1$
$\text{Al}_3\text{M}_{14}$	O	BCC/B2	$17.7 \pm 0.7$	$20.7 \pm 0.8$	$21.0 \pm 0.8$	$20.8 \pm 0.6$	$19.8 \pm 0.7$

<sup>a</sup> O: overall, DR: dendritic region, ID: inter-dendritic region.

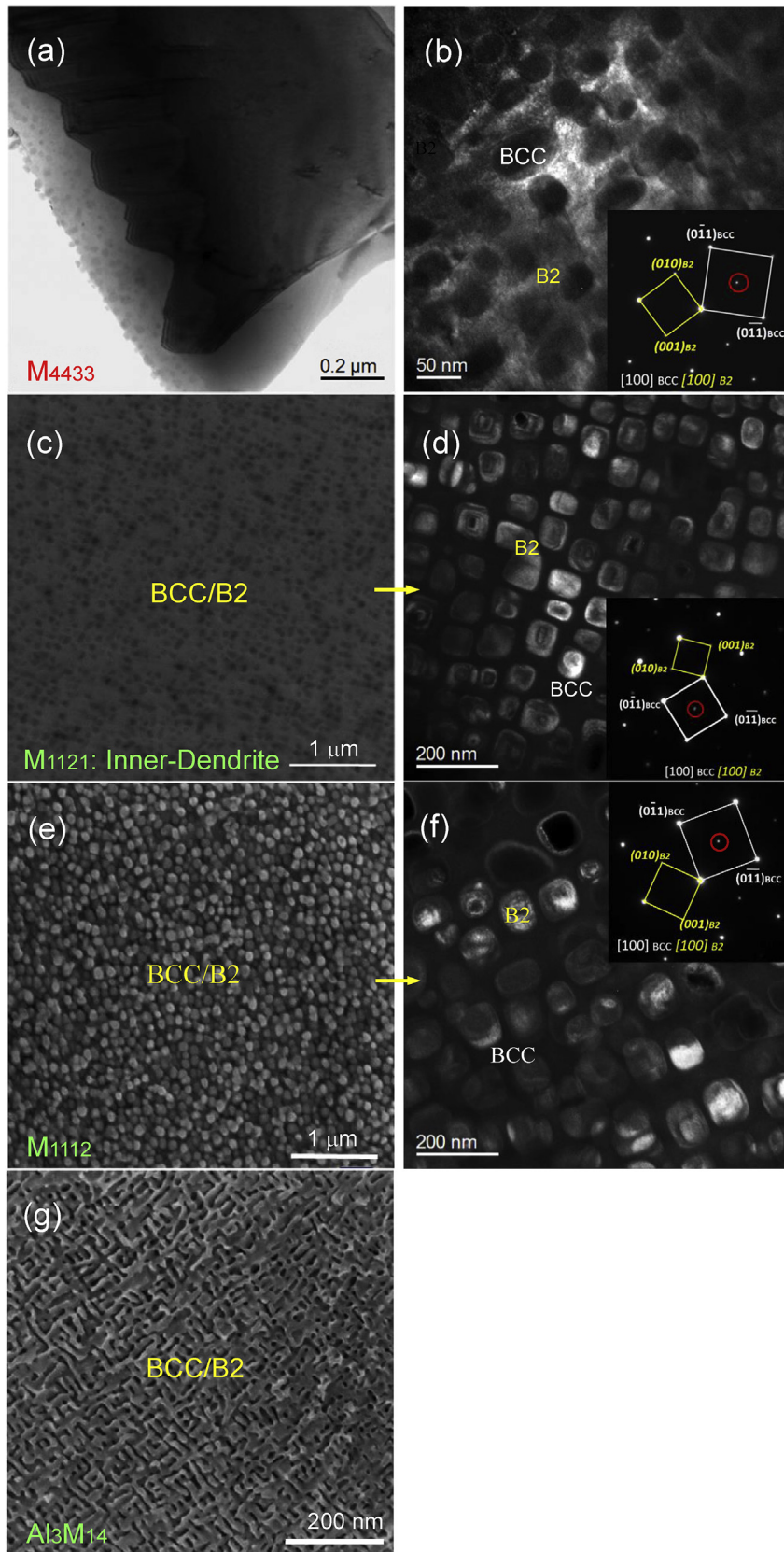


**Fig. 3.** TEM images of the as-cast  $M_{4433}$  (a, b), in which the dark-field image of the BCC/B2 region shows that BCC particles are embedded in the B2 matrix; (c): SEM image of the coarse columnar dendrites in  $M_{1121}$ , in which nanoparticles are identified by the dark-field TEM analysis (d) as the cuboidal B2 particles in BCC matrix; (e): SEM image of  $M_{1112}$ , showing the cuboidal particles are distributed in the matrix, which are identified by the dark-field TEM analysis (f) as cuboidal B2 particles in BCC matrix; (g): SEM image of  $Al_3M_{14}$  HEA showing a weave-like morphology.

dual-phase (FCC+BCC) structure before.

On the other hand, in the BCC-dominant HEA  $M_{1121}$ , observed coarse columnar dendrites actually consists of a disordered BCC matrix and uniformly-dispersed nanoparticles (dark phase in Fig. 3c). TEM dark-field image taken from the dendritic region (Fig. 3d) shows that these cuboidal nanoparticles with a size of about 50–100 nm are B2 particles coherently embedded in the BCC matrix, as indicated by the SAED pattern (inset of Fig. 3d). This intriguing morphology is notably similar to that observed in the Ni-base superalloys, namely, a uniform dispersion of coherent cuboidal ordered  $\gamma'$  ( $L1_2$ -Ni<sub>3</sub>Al) particles in the parent FCC  $\gamma$  matrix [37,38]. At increasing the Cr content instead of Fe, the FCC phase completely disappears in  $M_{1112}$  and the alloy shows a microstructure consisting of the dispersion of cuboidal B2 nanoparticles (bright phase) with a size of about 80–120 nm that are coherent with the BCC matrix, as indicated by the SAED pattern (Fig. 3e and f). In comparison, when the Al content is varied from  $Al_2M_{14}$  (12.5 at. % Al) to  $Al_3M_{14}$  (17.6 at. % Al), instead of mutating the TMs, a weave-like spinodal decomposition of B2 and BCC begins to occur (Fig. 3g), leading to a brittle alloy. It is particularly noted that, no matter an alloy has a BCC or FCC-dominant structure, interfacial

coherency between BCC and B2 is always retained, although the exact morphology of phase distribution in different regions strongly depends on the chemical compositions of the alloy.

The interface between BCC and B2 was further examined using a high-resolution TEM (HRTEM) and the results are given in Fig. 4a, in which a mixture of BCC and B2 phases in  $M_{1112}$  alloy is shown. The fast Fourier transformation (FFT) patterns of a B2 (Fig. 4b), BCC (Fig. 4c), and another B2 (Fig. 4d), indicate the (100) atomic planes of B2 particles. An enlarged image (Fig. 4e) and its corresponding schematic illustration (Fig. 4f) clearly reveal the interfacial coherence between the BCC matrix and B2 particles. We also made effort to map the chemical distribution of elements in the BCC/B2 regions using STEM and the results are given in Fig. 5. It shows that Al and Ni are enriched in the B2 particles, but depleted in the BCC matrix. In addition, while Fe, Co, and Cr are preferentially segregated in the BCC matrix.

#### 4.2. Mechanical properties

To examine the effect of microstructure on mechanical properties, both uniaxial tension and compression tests were conducted.

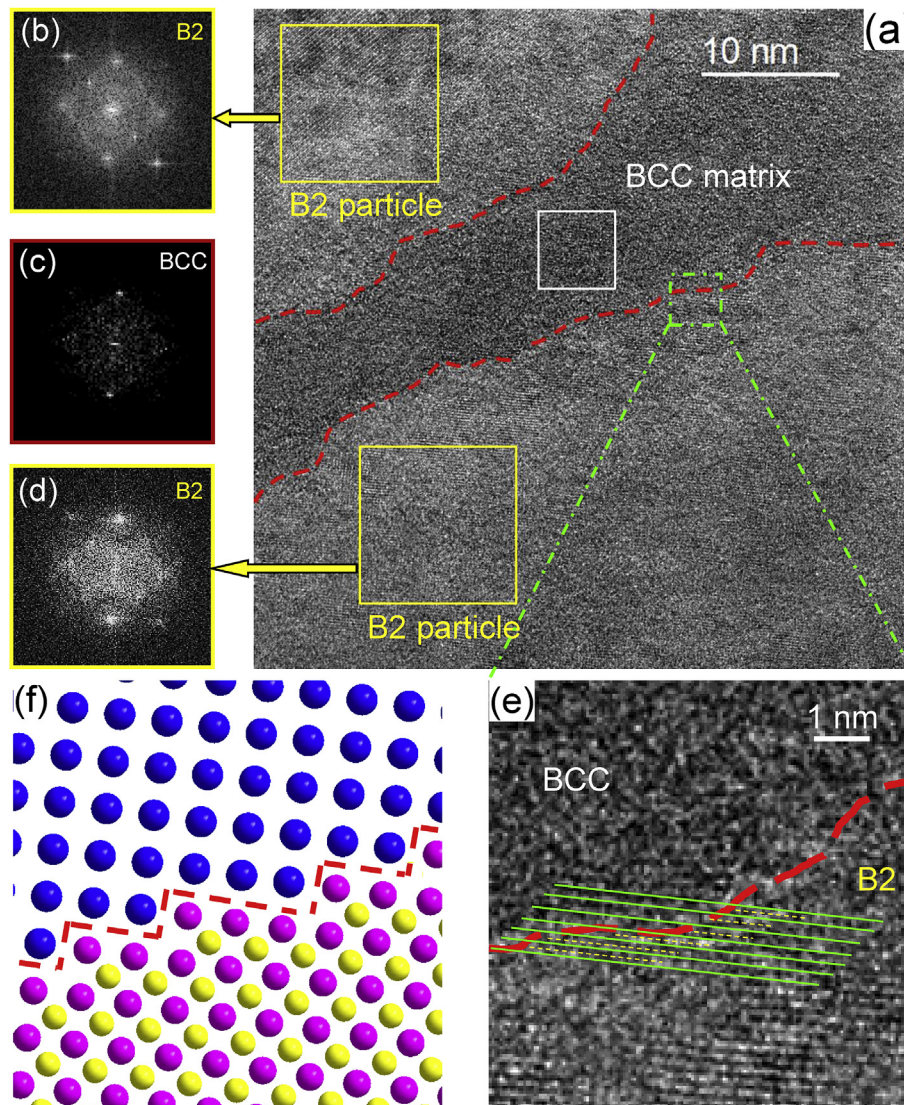


**Fig. 4.** HRTEM images of  $M_{1121}$  alloy. (a): A HRTEM image showing the interfaces between the BCC matrix and two B2 particles with FFT patterns of B2 (b), BCC (c) and B2 (d), respectively; (e): A high-magnification HRTEM image caught from (a), showing details of the BCC/B2 interface; (f): Diagrammatic sketch of (e).

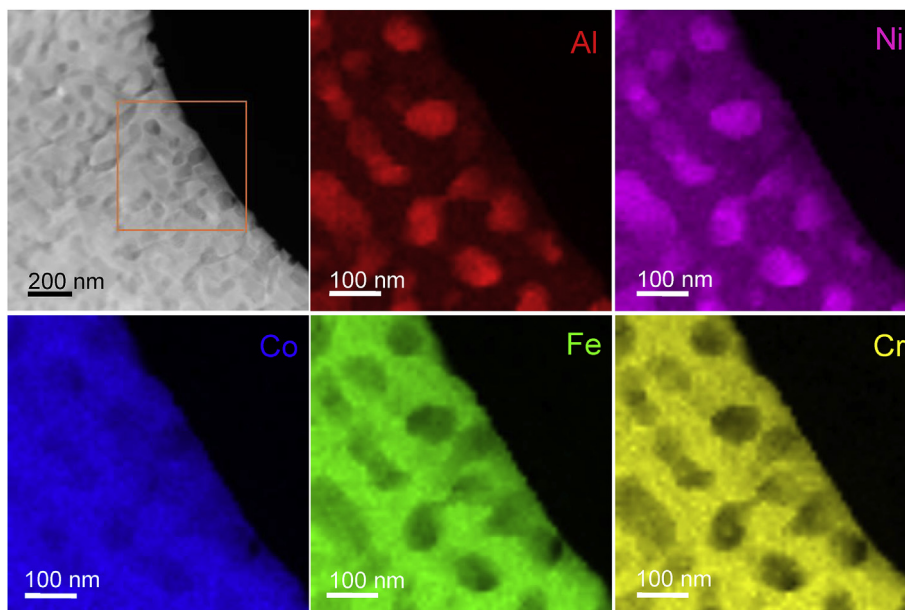


Fig. 5. The elemental distribution in the BCC/B2 region of  $M_{1121}$  alloy mapped with STEM.

Engineering tensile stress-strain curves of the current five HEAs tested at the room temperature are depicted in Fig. 6a. Tensile yield strengths ( $\sigma_y^t$ ), ultimate tensile strength ( $\sigma_{UTS}^t$ ), and uniform elongation ( $\delta$ ) corresponding to  $\sigma_{UTS}^t$  of these alloys are listed in Table 1. The two FCC-dominant HEAs,  $M_{1111}$  and  $M_{4433}$ , exhibit large tensile plasticity and, in particular,  $M_{4433}$  is noted to deform significantly without fracture, even beyond the displacement limit preset by our test machine ( $\delta > 33\%$ ). Interestingly, these ductile alloys do not show macroscopic sample necking prior to fracture. In other words, their ductility values are the same as uniform elongation. Yield strengths of the FCC-dominant alloys are generally lower than that of BCC-dominant alloys. For example,  $M_{1121}$  has a high strength of  $\sigma_y^t = 991$  MPa and a lower ductility of  $\delta = 8.2\%$ . However, in the case of BCC-structured  $M_{1112}$  and  $Al_3M_{14}$ , alloys appear to be completely brittle. In fact, these two alloys exhibit cleavage fracture before reaching the yielding point. The brittleness is related to casting defects, as will be discussed in the next section.

In order to obtain the yield strengths of brittle  $M_{1112}$  and  $Al_3M_{14}$  alloys and to investigate possible yield asymmetry, compression tests were conducted on all alloys and their true stress-strain curves are shown in Fig. 6b. Compressive yield strengths ( $\sigma_y^c$ ) of the studied alloys are also listed in Table 1, from which it is observed that the  $\sigma_y^c$  is comparable with the  $\sigma_y^t$ , with the former only slightly higher (~5–8%) than the latter. Compressive yield strength of the FCC-dominant  $M_{4433}$ , can be apparently enhanced by the insertion of inter-dendritic BCC/B2 phase, for example, from 387 MPa in  $M_{4433}$  to 614 MPa in  $M_{1111}$ , as a result of increasing BCC/B2 phase content from 15% to 35% (in volume fraction). When the BCC structure becomes dominant, such as in  $M_{1121}$  which contains about 25% of the FCC phase, the compressive yield strength jumps sharply to 1085 MPa. In fact, the strength of the single-phase, BCC-structured  $M_{1112}$  even reaches a higher value of  $\sigma_y^c = 1718$  MPa, about 3–4 times of the value for the FCC-dominant HEAs. In comparison, the BCC Al-rich  $Al_3M_{14}$  alloy has a weave-like BCC/B2 microstructure exhibits a lower yield strength of 1399 MPa.

We also performed microhardness ( $HV$ ) measurements on various samples and the results are listed in Table 1.  $HV$  varies, depending on the structure of alloys. As shown in Fig. 7, the measured  $HV$  value scales linearly with the yield strength, obeying

the traditional Tabor relation [52], namely  $HV = \alpha \cdot \sigma_y$ , with the proportional coefficient  $\alpha$  being about 3.3.

#### 4.3. Fracture surfaces

Fracture surfaces of samples after tension tests were examined by SEM, as shown in Fig. 8. For the high-strength BCC-structured  $M_{1112}$  and  $Al_3M_{14}$ , the fracture morphologies exhibit quasi-cleavage river-pattern characteristics, indicating brittle materials (Fig. 8a and b). For  $M_{1112}$  (B2 particle-reinforced BCC matrix), crack always initiates from a cast void. Several attempts were made to suction cast  $M_{1112}$ , but viscosity of the melt was apparently too high to prohibit the synthesis of defect-free samples. Therefore, the observed fracture mode may not represent the true, intrinsic feature. Nonetheless, based on its extremely high yield strength, the alloy is not expected to be ductile. For  $Al_3M_{14}$ , the cleavage fracture in  $Al_3M_{14}$  might be induced by the weave-like spinodal decomposition, as shown in the high-magnification fractography in Fig. 8b, in which the modulated structure is readily visible.

By contrast, the fracture surfaces of mixed BCC-FCC structured  $M_{1121}$  have numerous dimples after tension, indicating a large plasticity (Fig. 8c). In addition, the TEM image (Fig. 6c) also shows the presence of a large amount of dislocations in the inner-dendritic region (microstructure: cuboidal B2 precipitates dispersed in BCC matrix) in the  $M_{1121}$  after tension, indicating a large plastic flow in BCC/B2 region. Notably, tangled dislocations are also observed in the BCC/B2  $M_{1112}$  sample after compression, as shown in Fig. 6d. For the ductile FCC-based  $M_{1111}$ , a typical dimple morphology is revealed on the fracture surface, as shown in Fig. 8d.

#### 4.4. Precipitate stability

Microstructural stability of  $M_{1112}$  which contains cuboidal coherent precipitates is examined. Samples were initially heat-treated at temperatures ranging from 673 to 1073 K for 2 h and, then, followed by water-quenching. The resulting microstructures are presented in Fig. 9. It appears that the cuboidal morphology of the B2 nanoprecipitates is maintained up to 873 K (Fig. 9a and b), below which the only obvious change is the gradual increase of the

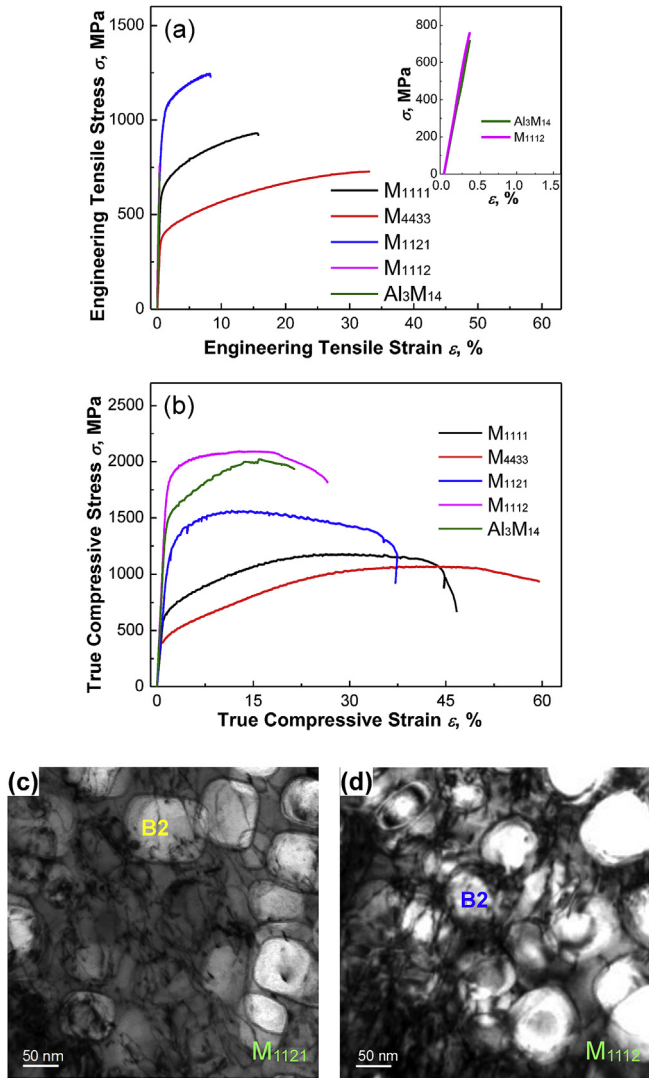


**Fig. 6.** Engineering tensile (a) and true compressive (b) stress-strain curves of  $Al_2M_{14}$  and  $Al_3M_{14}$  HEAs. TEM morphologies of  $M_{1121}$  after tension and  $M_{1112}$  after compression are shown in (c) and (d), respectively.

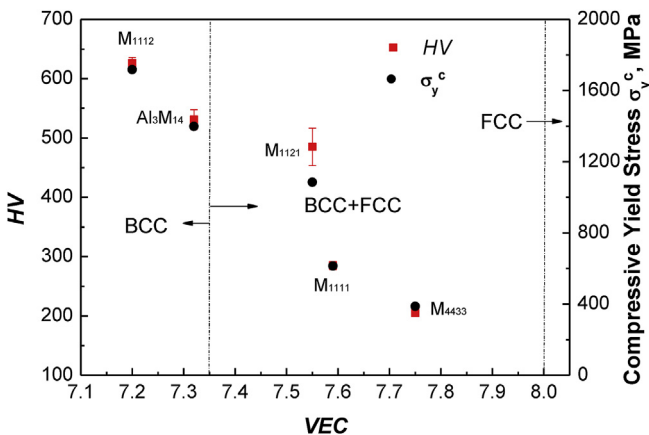


**Fig. 7.** Variations of compressive yield strength  $\sigma_y^c$ , microhardness  $HV$  and crystal structures with  $VEC$  of the designed HEAs.

size of B2 particles with the annealing temperature, for example, from 70–110 nm at 673 K to 110–160 nm at 873 K. At a temperature

above 973 K, however, B2 particles begin to raft, as seen in Fig. 9c and d, indicating the loss of stability. Worse yet, the notorious brittle  $\sigma$  phase ( $tP$ -FeCr) with a tetragonal structure begins to appear at  $T > 873$  K, as identified by the XRD result in Fig. 10a. It is a result of destabilization of the coherent microstructure. In fact, the BCC matrix is gradually replaced by the growth of  $\sigma$  phase with increasing temperature, since the BCC matrix is enriched with Fe, Co, and Cr, as demonstrated by the STEM results (Fig. 5). This result agrees with the notion that, in many stainless steels, the segregation of Fe and Cr can accelerate the formation of  $\sigma$  phase within the temperature range of 773–1073 K [53]. Our microhardness data as a function of temperature also affirm this phase transition of BCC to  $\sigma$ . As shown in Fig. 10b, the microhardness value of the heat-treated  $M_{1112}$  below 873 K remains almost constant at  $HV = 626$ , but increases drastically to a high value of  $HV = 850$  when the temperature is above 873 K. Therefore, it may be concluded that, in this series of Al-Ni-Co-Fe-Cr HEAs, the microstructure of cuboidal coherent precipitation is stable below 873 K, beyond which brittle  $\sigma$  phase begins to appear inevitably due to the excessive Fe and Cr in the BCC regions.

## 5. Discussion

### 5.1. Structural evolution and strength of $Al_2M_{14}$ HEAs

Several parameters, such as atomic size and enthalpy of mixing, have been proposed to affect the phase structure formation in HEAs [54,55]. For instance, adding foreign element with larger atomic size is expected to distort the crystal lattice, thus destabilize a close-packed FCC structure and to promote the formation of loose-packed BCC structure [56], for example, the addition of large Al atom into FCC-NiCoFeCr(Mn) alloy [57]. The electron concentration is another factor that can affect the phase stability via the interaction between the Fermi surface in real space and the Brillouin zone in the reciprocal space [58]. In this case, since it is often difficult to obtain the exact value of the valence electrons per atom in a multicomponent system, the valence electron concentration (VEC), i.e.,  $VEC = \sum_{i=1}^n c_i (VEC)_i$ , where  $c_i$  is the atomic percentage and  $(VEC)_i$  is the VEC value of the  $i^{th}$  element, is adopted. Several efforts have been also made to determine the stability of FCC and BCC HEAs using this empirical parameter [59].

In the present study, we adopted the latter method and found that our HEA series with  $VEC < 7.35$  exhibit a single BCC/B2 solid solution structure, and HEAs with  $7.35 < VEC < 8.0$  have a dual-phase of (FCC + BCC); this is shown in Fig. 7. The tendency of the structural evolution with the VEC, by mutating the TMs, is actually quite similar to that by varying the Al content. The slight difference seems to be the exact VEC values for defining the phase regions, namely, the dual-phase region in the present alloy series is slightly narrower comparing with that ( $6.87 < VEC < 8.0$ ) in the literature [59].

To correlate the mechanical strength with the crystal structure, variations of compressive  $\sigma_y$  and  $HV$  as a function of VEC for the currently-studied five HEAs are plotted in Fig. 7. For easy discussion, various phase boundaries are also drawn. Both  $\sigma_y$  and  $HV$  are noted to decrease as the VEC value increases and the single-phase BCC alloys ( $M_{1112}$  and  $Al_3M_{14}$ ) have the highest strength and hardness. By contrast, the FCC-dominated alloys ( $M_{1111}$  and  $M_{4433}$ ) have the lowest strength, but with a much better ductility (Fig. 6a). From a practical point of view, the dual-phase HEAs seem to have a more balanced strength-ductility property. These results demonstrate that the mutation of transition metals in the  $Al_2M_{14}$  HEAs, instead of only adding Al, is also able to produce similar effects on the phase structures in HEAs. In fact, high tensile strength and good ductility in some special HEAs, e.g.,  $M_{1121}$ , seems tunable. The present results

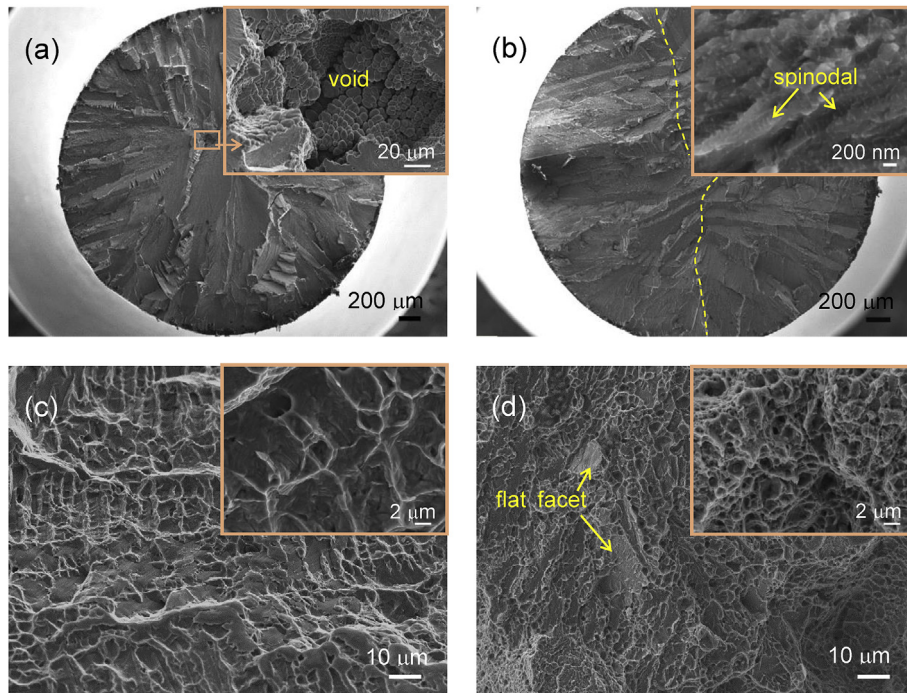


**Fig. 8.** SEM fractographies of various HEAs after tension, including  $M_{1112}$  (a),  $Al_3M_{14}$  (b),  $M_{1111}$  (c) and  $M_{1121}$  (d).

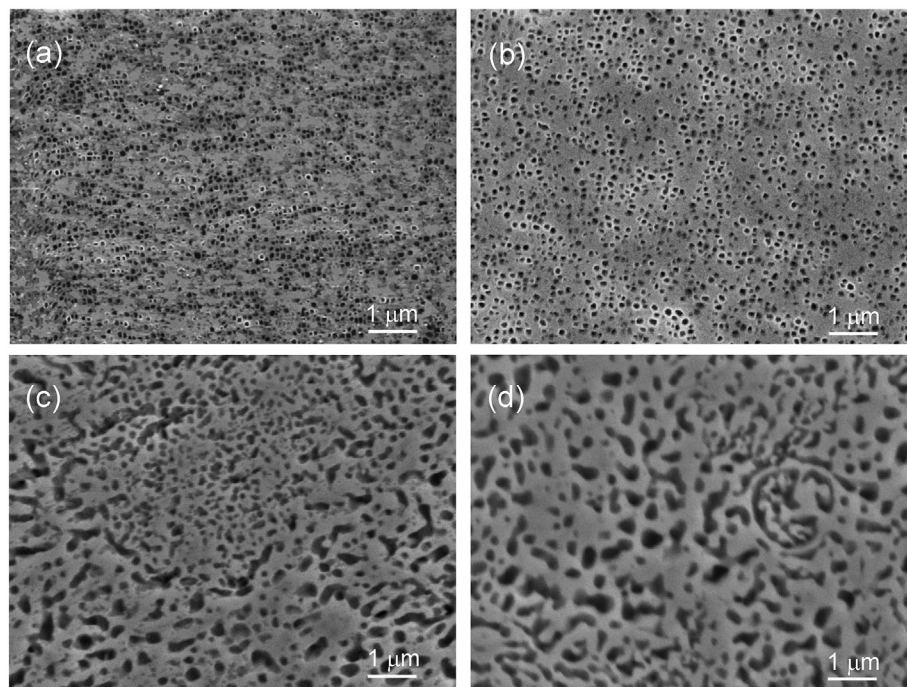


**Fig. 9.** SEM images of  $M_{1112}$  annealed at 673 K (a), 873 K (b), 973 K (c), and 1073 K (d) for 2 h, respectively.

also indicate that  $VEC$  is a practical parameter to evaluate structural stability in HEAs designed by the current composition formula approach.

It is especially noted that, in this  $Al_2M_{14}$  HEA series, the presence of the BCC phase is always accompanied by the coherent B2 phase, which contributes to the strengthening of the alloys. In the following, we will discuss microstructural variables that determine the formation and morphology of these coherent precipitates.

## 5.2. Formation of cuboidal coherent precipitates

From both the SEM and TEM observations (Fig. 3), we found that, no matter it is in FCC- or BCC-dominant HEAs, ordered B2 phase always appeared together with the BCC phase. For instance, in the inter-dendritic regions of the FCC-dominant  $M_{4433}$  alloy, the ellipsoidal BCC nanoparticles were embedded coherently in the ordered B2 matrix (Fig. 3a and b). The presence of BCC/B2 region is

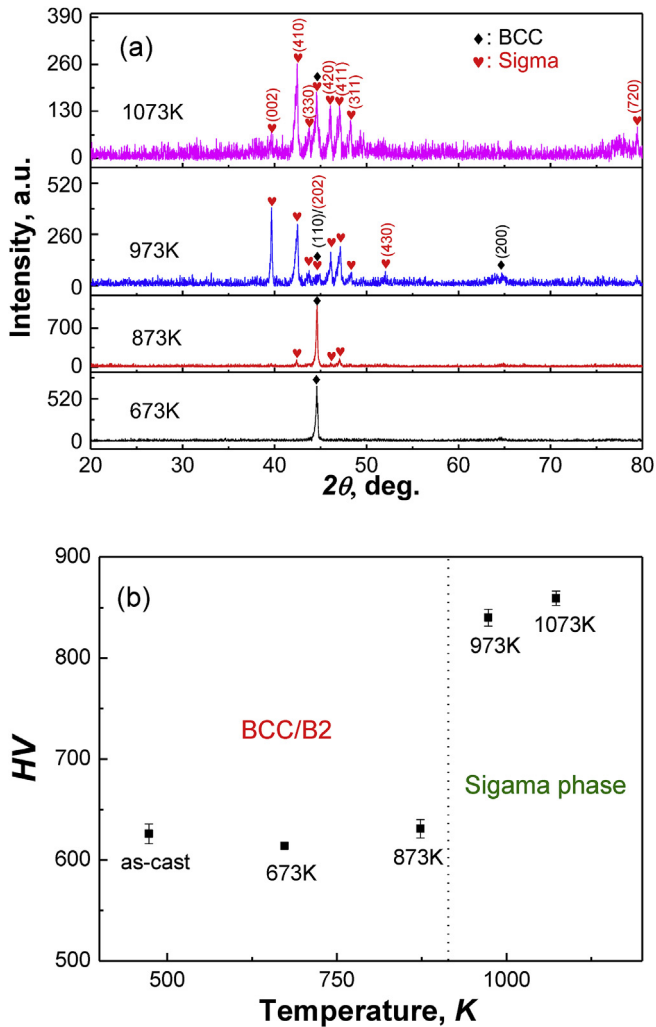


Fig. 10. XRD patterns (a) and microhardness HV (b) of M<sub>1112</sub> annealed at different temperatures.

apparently resulted from a high Al content, as evidenced by the fact that the composition of this region is Al<sub>21.2</sub>Ni<sub>29.9</sub>Co<sub>21.1</sub>Fe<sub>13.8</sub>Cr<sub>14.0</sub> (at. %, Table 2). On the other hand, in the BCC-dominant M<sub>1121</sub> alloy, ordered cuboidal B2 nanoparticles are observed to coherently disperse in the dendritic BCC matrix (Fig. 3c and d). Interestingly, similar morphology is also observed in the single-phase BCC M<sub>1112</sub> alloy (Fig. 3e and f). Largely different from the Al<sub>2</sub>M<sub>14</sub> family, the

high-Al HEA Al<sub>3</sub>M<sub>14</sub> shows a spinodal weave-like microstructure (Fig. 3g), often observed in single BCC HEAs with a high Al content [60].

In principle, the equilibrium shape of coherent precipitates is determined by minimizing the sum of the elastic and interfacial energies [61–64]. The interface contribution to the total precipitate energy scales with precipitate surface area, generally dominates the shape of small-sized particles. On the other hand, the elastic energy, which is resulted from the lattice misfit accommodation across the coherent interface, scales with the volume of particles and dominates the shape of large-sized particles. Thus, the shape is a function of the particle size. For example, the shape of Al<sub>3</sub>Sc coherent particles in (Al, Sc)-based alloys changes from sphere to cuboid and, then, plate as the particle size continuously increases [64]. The relative importance of the elastic energy and the interfacial energy is evaluated through the characteristic parameter  $L$ , i.e.,  $L = \frac{\epsilon^2 C_{44} r}{s}$ , where  $\epsilon$  is the lattice misfit,  $C_{44}$  is the elastic constant of the matrix,  $r$  is the average particle size (the diameter of spherical particle or the length of cuboidal particle), and  $s$  is the average specific interfacial energy. It has been reported [61–64] that a small  $L$  usually corresponds to a spherical particle, which transforms to ellipsoidal or cuboidal shape when  $L$  increases. At a larger  $L$ , the fourfold symmetry of cuboidal particles is broken and some low symmetric shapes, like plates, begin to appear.

In this study, the lattice misfit  $\epsilon$  between BCC and B2 phases is calculated using the equation of  $\epsilon = 2 \times (a_{B2} - a_{BCC}) / (a_{B2} + a_{BCC})$ , where  $a_{B2}$  and  $a_{BCC}$  are the lattice constants of B2 and BCC, respectively. The lattice constants  $a$ , lattice misfit  $\epsilon$ , particle size  $r$ , and the characteristic parameter  $L$  of the current HEAs are summarized in Table 3, in which the  $C_{44}$  and  $s$  values for the BCC/B2 alloys are taken from those of B2-NiAl phase, being  $C_{44} = 130$  GPa and  $s = 0.125$  J/m<sup>2</sup> [65–67]. The ellipsoid-shaped BCC nanoprecipitates observed in the inter-dendritic BCC/B2 regions of the M<sub>4433</sub> alloy appear to result from a small  $L$  value ( $L = 0.2$ ). Since particle sizes in all Al<sub>2</sub>M<sub>14</sub> HEAs are comparable, the lattice misfit  $\epsilon$  must play the key role in determining the shape of these particles. Along this line, the ellipsoidal shape of precipitates in M<sub>4433</sub> is a result of a small lattice misfit of  $\epsilon = 0.17\%$ . In comparison, the BCC-dominant M<sub>1121</sub> alloy has a moderate  $\epsilon$  of  $-0.38\%$ , thus leading to the formation of coherent cuboidal B2 precipitates. In the single-phase BCC-M<sub>1112</sub> alloy, a slightly-high lattice misfit of  $\epsilon = 0.45\%$  still render the alloy with coherent cuboidal B2 nanoparticles (Fig. 3e and f) with a larger particle size (80–120 nm) and a higher volume fraction (53–57%), as compared to the B2 particles in M<sub>1121</sub>. When the lattice misfit is further increased, for example in the single-phase BCC-Al<sub>3</sub>M<sub>14</sub> alloy with  $\epsilon = 0.63\%$  (Al content is higher than that in Al<sub>2</sub>M<sub>14</sub>), a weave-like morphology is formed. The  $L$  value for Al<sub>3</sub>M<sub>14</sub> is not available because the great difficulty of measuring the particle size at this

Table 3

Lattice constants ( $a_{B2}$  and  $a_{BCC}$ ) of the ordered B2 and its parent BCC matrix, lattice misfits  $\epsilon$ , average sizes ( $r$ ) of precipitates (the diameter of spherical particle or the length of cuboidal particle), and the parameter  $L$  (related to the shape of precipitates) in the designed Al<sub>2</sub>M<sub>14</sub> and Al<sub>3</sub>M<sub>14</sub> HEAs.

	Chemical compositions (at. %)	$a_{B2}$ (Å)	$a_{BCC}$ (Å)	$\epsilon$ (%)	$r$ (nm)	$L^a$ ( $10^{-1}$ )
M <sub>1111</sub>	Al <sub>12.5</sub> Ni <sub>21.875</sub> Co <sub>21.875</sub> Fe <sub>21.875</sub> Cr <sub>21.875</sub>	2.871 ±0.007	2.854 ±0.006	0.59 ±0.15	–	–
M <sub>4433</sub>	Al <sub>12.5</sub> Ni <sub>25</sub> Co <sub>25</sub> Fe <sub>18.75</sub> Cr <sub>18.75</sub>	2.876 ±0.004	2.871 ±0.002	0.17 ±0.08	60	0.2
M <sub>1121</sub>	Al <sub>12.5</sub> Ni <sub>17.5</sub> Co <sub>17.5</sub> Fe <sub>35</sub> Cr <sub>17.5</sub>	2.851 ±0.005	2.862 ±0.004	$-0.38 \pm 0.07$	70	1.1
M <sub>1112</sub>	Al <sub>12.5</sub> Ni <sub>17.5</sub> Co <sub>17.5</sub> Fe <sub>17.5</sub> Cr <sub>35</sub>	2.869 ±0.006	2.856 ±0.003	0.45 ±0.11	100	2.1
Al <sub>3</sub> M <sub>14</sub>	Al <sub>17.64</sub> Ni <sub>20.59</sub> Co <sub>20.59</sub> Fe <sub>20.59</sub> Cr <sub>20.59</sub>	2.884 ±0.005	2.866 ±0.004	0.63 ±0.17	–	–

<sup>a</sup>  $L = \frac{\epsilon^2 C_{44} r}{s}$ , in which  $C_{44} = 130$  GPa and  $s = 0.125$  J/m<sup>2</sup> for BCC/B2 alloys [65–67].

state. However, in an analogy, the observation of spinodal microstructure reported in the high Al-containing BCC- $\text{Al}_x\text{NiCoFeCr}$  ( $x > 0.7$ ) might be attributable to a high lattice misfit [31,35].

The morphology of secondary phase apparently has a profound effect on the mechanical properties. For example, although both  $\text{M}_{1112}$  and  $\text{Al}_3\text{M}_{14}$  have a single BCC structure, the compressive yield strength of  $\text{M}_{1112}$  alloy is higher than that of the  $\text{Al}_3\text{M}_{14}$  ( $\text{M}_{1112}$ :  $\sigma_y^c = 1718$  MPa;  $\text{Al}_3\text{M}_{14}$ :  $\sigma_y^c = 1399$  MPa, in Table 1). The strength difference is obviously caused by different microstructures composed of BCC and B2 phases, specifically, the former contains cuboidal coherent precipitates, but the latter has a weave-like morphology. The fact that a large amount of dislocations was observed in the BCC phase and terminated at the BCC/B2 interfaces in  $\text{M}_{1112}$  after compression (Fig. 4d) and in  $\text{M}_{1121}$  alloy after tension (Fig. 4c) indicated that extensive plasticity has occurred in these samples. Notably, such dislocation structure was also frequently observed in  $\gamma/\gamma'$ -type Ni-based superalloys [37,38] which had a uniform distribution of cuboidal coherent precipitates. In the current case, the desirable microstructure is produced by varying the combinations of transition metals, thus tuning the lattice misfit.

### 5.3. Strengthening effect by coherent-precipitates

The mechanism for precipitation strengthening can be divided into two categories, Orowan bowing or particle shearing, depending on the interaction between moving dislocations and precipitates. Orowan mechanism generally occurs when the particles are large or incoherent with the matrix, while the shearing mechanism dominates when the precipitates are coherent and small. For the coherent precipitation, three factors contribute to the increase in yield strength, coherency strengthening ( $\Delta\sigma_{CS}$ ), modulus mismatch strengthening ( $\Delta\sigma_{MS}$ ), and order strengthening ( $\Delta\sigma_{OS}$ ). These strengthening processes are sequential, the former two ( $\Delta\sigma_{CS}$  and  $\Delta\sigma_{MS}$ ) occur prior to the shearing of precipitates by dislocations, and the latter one ( $\Delta\sigma_{OS}$ ) during the shearing. In this case, the larger of ( $\Delta\sigma_{CS} + \Delta\sigma_{MS}$ ) or  $\Delta\sigma_{OS}$  is expected to be the total strength increment from the shearing mechanism. The equations available to calculate these strength increments are [68–74]:

$$\Delta\sigma_{CS} = M \cdot \alpha_\epsilon \cdot (G\epsilon_c)^{\frac{3}{2}} \cdot \left(\frac{rf}{0.5Gb}\right)^{\frac{1}{2}}, \quad (1)$$

$$\Delta\sigma_{MS} = M \cdot 0.0055 \cdot (\Delta G)^{\frac{3}{2}} \cdot \left(\frac{2f}{G}\right)^{\frac{1}{2}} \cdot \left(\frac{r}{b}\right)^{\frac{3m-1}{2}}, \quad (2)$$

$$\Delta\sigma_{OS} = M \cdot 0.81 \cdot \frac{\gamma_{apb}}{2b} \cdot \left(\frac{3\pi f}{8}\right)^{\frac{1}{2}}, \quad (3)$$

where  $M = 2.73$  for BCC structure and 3.06 for FCC structure (Taylor Factor) [52],  $\alpha_\epsilon = 2.6$  (a constant) [70,71],  $m = 0.85$  (a constant) [72,73],  $\epsilon_c = 2\epsilon/3$  [69–71], the constrained lattice misfit.  $G$  and  $\Delta G$  are the shear modulus of the matrix and the shear modulus

mismatch between precipitates and matrix, respectively;  $b$  is the Burgers vector;  $r$  is the average particle size and  $f$  is the volume fraction of the precipitates, respectively;  $\gamma_{apb}$  is the anti-phase boundary energy of the precipitates.

By applying these equations, the strength increments of  $\Delta\sigma_{CS}$ ,  $\Delta\sigma_{MS}$ , and  $\Delta\sigma_{OS}$  in the BCC  $\text{M}_{1112}$  alloy containing B2 nano-precipitates are calculated to be  $\Delta\sigma_{CS} = 2041$  MPa,  $\Delta\sigma_{MS} = 46$  MPa, and  $\Delta\sigma_{OS} = 900$  MPa, respectively. Parameters used for calculations are  $G = 83$  GPa (for  $\alpha$ -Fe) [75],  $b = \sqrt{3} \times a_{\text{BCC}}/2 = 0.2473$  nm,  $r = 100$  nm,  $f = 0.55$ ,  $\Delta G = 83 - 80 = 3$  GPa (the shear modulus of B2-NiAl is  $G = 80$  GPa [65]), and  $\gamma_{apb} = 0.25$  J/m<sup>2</sup> [66], which are also listed in Table 4. The strength increment  $\Delta\sigma_{OS}$  from the order strengthening is noted to be less than ( $\Delta\sigma_{CS} + \Delta\sigma_{MS}$ ) from coherency strengthening and modulus mismatch, suggesting the coherency strengthening dominates when the size of coherent precipitates is large ( $> 40$  nm) [10,11]. The same case also occurs in BCC-structured  $\text{M}_{1121}$  alloy.

It should be pointed out that the magnitude of ( $\Delta\sigma_{CS} + \Delta\sigma_{MS}$ ) is functions of  $r$ ,  $f$ , and, especially, the lattice misfit  $\epsilon$ . In this case, since the shearing and bypassing mechanisms occur concurrently and are independent to each other, the strengthening is determined by the smaller of ( $\Delta\sigma_{CS} + \Delta\sigma_{MS}$ ) or  $\Delta\sigma_{orowan}$ . In other words, the softer yield strength increment could be reached when ( $\Delta\sigma_{CS} + \Delta\sigma_{MS}$ ) =  $\Delta\sigma_{orowan}$  at a critical particle size  $r_0$  with a fixed  $f$ . The strength increment  $\Delta\sigma_{orowan}$  is governed by the dislocation bypassing mechanism and can be calculated with the equation [52,76–78]:

$$\Delta\sigma_{orowan} = M \cdot \frac{0.4Gb}{\pi\sqrt{1-\nu}} \cdot \frac{\ln\left(2\sqrt{\frac{2}{3}}r/b\right)}{\lambda_p} \quad (4)$$

$$\lambda_p = 2\sqrt{\frac{2}{3}}r \left(\sqrt{\frac{\pi}{4f}} - 1\right),$$

where  $\nu$  is the Poisson ratio ( $\nu = 0.3$  for the BCC HEAs [52]), and  $\lambda_p$  is the inter-precipitate spacing. Thereof, the calculated critical size of the B2 cuboids in  $\text{M}_{1112}$  HEA is  $r_0 = 88$  nm, which is actually quite consistent with the experimental average value of  $r = 100$  nm. Similarly, in the case of  $\text{M}_{1121}$  alloy, the experimental size  $r = 70$  nm of the cuboidal B2 particles is also close to the optimal value of  $r_0 = 60$  nm. In both alloys, the largest strength increment was obtained not only through the optimization of the particle size but also through a uniform dispersion of these coherent particles in the matrix.

In perspective, strengthening caused by the two mechanisms, ( $\Delta\sigma_{CS} + \Delta\sigma_{MS}$ ) and  $\Delta\sigma_{orowan}$ , are plotted as a function of  $r$  for the current BCC  $\text{M}_{1121}$  and  $\text{M}_{1112}$  HEAs, as shown in Fig. 11. For comparison, calculations for precipitation-hardened FCC-(FeCoNiCr)<sub>94</sub>-Ti<sub>2</sub>Al<sub>4</sub> HEA (at. %) are also included [10]. Material parameters used for the calculations are listed in Table 4. It is of interest to note that the experimentally-measured particle size  $r$  is almost the same as

**Table 4**

Data used for the strength calculations.  $M$ : Taylor factor;  $G$ : shear modulus of matrix;  $b$ : Burger's vector;  $\nu$ : Poisson ratio;  $\epsilon$ : lattice misfit between the precipitate and the matrix;  $r$ : average size of precipitates;  $f$ : average volume fraction of precipitates;  $r_0$ : the optimal size of precipitates for the maximum strength increment.

Alloys	$M$ [52]	$G$ (GPa)	$b$ (nm)	$\nu$	$\epsilon$ (%)	$f$	$r$ (nm)	$r_0$ (nm)
$\text{M}_{1121}$ ( $\text{Al}_{12.5}\text{Ni}_{17.5}\text{Co}_{17.5}\text{Fe}_{35}\text{Cr}_{17.5}$ at. %)	2.73	83 [75]	0.2478	0.30 [52]	-0.38	0.4	70	60
$\text{M}_{1112}$ ( $\text{Al}_{12.5}\text{Ni}_{17.5}\text{Co}_{17.5}\text{Fe}_{35}\text{Cr}_{17.5}$ at. %)	2.73	83 [75]	0.2473	0.30 [52]	0.45	0.55	100	88
(FeCoNiCr) <sub>94</sub> Ti <sub>2</sub> Al <sub>4</sub> (at. %) [10]	3.06	81 [79]	0.2550	0.33 [79]	0.26	0.233	25	66

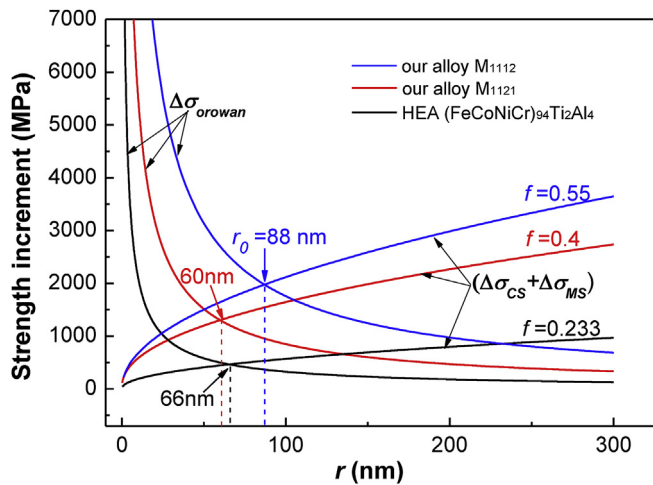


**Fig. 11.** Computations of  $(\Delta\sigma_{CS} + \Delta\sigma_{MS})$  and  $\Delta\sigma_{Orowan}$  as a function of particle size  $r$  for the present  $M_{1121}$ ,  $M_{1112}$  HEAs and another precipitation-hardened HEA [10]. The optimal particle sizes ( $r_0$ ) are marked for each alloy.

the theoretically-predicted  $r_0$  for the present two HEAs. However, in the case of FCC-(FeCoNiCr)<sub>94</sub>Ti<sub>2</sub>Al<sub>4</sub> HEA, the strength increment  $(\Delta\sigma_{CS} + \Delta\sigma_{MS})$  is only about half of the possible maximum value. The difference might be attributed to the fact that the practical particle size  $r = 25$  nm is much smaller than the optimal  $r_0 = 66$  nm.

## 6. Conclusions

In this study, the microstructural evolution, phase transition, formation of cuboidal precipitates, and mechanical properties of Al-Ni-Co-Fe-Cr HEAs based on the composition formula of Al<sub>2</sub>M<sub>14</sub> (M represents different mutations of the four transition metals) have been investigated. The following conclusions are drawn.

- 1) The phase formation and mechanical properties of these Al<sub>2</sub>M<sub>14</sub> HEAs are closely related to the valence electron concentration VEC. With decreasing VEC, the crystal structure switches from a dual-phase of (FCC + BCC/B2) to a single BCC/B2 phase, resulting in a drastic enhancement in strength at expense of ductility.
- 2) In either FCC or BCC-dominated Al<sub>2</sub>M<sub>14</sub> alloys, the BCC solid-solution phase is always accompanied by the presence of ordered B2 particles. In the BCC-dominated and single-phase BCC alloys, in particular, B2 particles are coherently distributed in the BCC solid-solution matrix.
- 3) The shape of coherent B2 precipitates is determined primarily by the lattice misfit  $\epsilon$  between the BCC matrix and B2 phase. A small  $\epsilon$  ( $\epsilon < 0.2\%$ ) results in spherical/ellipsoidal precipitates. At a moderate  $\epsilon$  ( $\epsilon \sim 0.4\%$ ), a microstructure with uniform distribution of coherent cuboidal B2 nanoprecipitates is obtained. At a large  $\epsilon$  ( $\epsilon > 0.6\%$ ), however, a weave-like microstructure is developed, which causes serious ductility loss.
- 4) We have calculated the strengthening effect predicted by the particle shearing and Orowan bowing mechanisms and the calculations are compared favorably with experiments. The lattice misfit parameter appears to be the most effective factor to control the strength of the alloy, and specifically an intermediate value of  $\epsilon \sim 0.4\%$  produces the strength maximum. For example, a single-phase BCC-Al<sub>2</sub>M<sub>14</sub> (M = Ni<sub>1</sub>Co<sub>1</sub>Fe<sub>1</sub>Cr<sub>2</sub>) with  $\epsilon = 0.45\%$  exhibits the highest compressive yield strength ( $\sigma_y^c = 1718$  MPa).
- 5) We have demonstrated that, by mutating the transition elements in Al<sub>2</sub>M<sub>14</sub> HEAs, the microstructure of Al-(Ni-Co-Fe-Cr)-

based alloys can be manipulated and controlled more flexibly than simply by adding Al alone. In perspective, the current design approach allows us to tune the lattice misfit and, subsequently, optimize the properties of precipitation-hardened HEAs.

## Acknowledgements

It was supported by the national key research and development plan (2017YFB0702400 and 2017YFB0306100), the Science Challenge Project (TZ2016004), the National Magnetic Confinement Fusion Energy Research Project (2015GB121004), the International Science & Technology Cooperation Program of China (2015DFR60370), the National Natural Science Foundation of China [No. U1610256]. TGN would like to acknowledge the financial support by US-NSF under contract DMR-1408722.

## References

- [1] O.N. Senkov, J.D. Miller, D.B. Miracle, C. Woodward, Accelerated exploration of multi-principal element alloys with solid solution phases, *Nature Commun* 6 (2015) 7529.
- [2] Y.F. Ye, Q. Wang, J. Lu, C.T. Liu, Y. Yang, High-entropy alloy: challenges and prospects, *Mater. Today* 19 (2016) 349–362.
- [3] D.B. Miracle, O.N. Senkov, A critical review of high entropy alloys and related concepts, *Acta Mater.* 122 (2016) 488–511.
- [4] J.W. Yeh, S.K. Chen, S.J. Lin, J.Y. Gan, T.S. Chin, T.T. Shun, C.H. Tsau, S.Y. Chang, Nanostructured high-entropy alloys with multiple principal elements: novel alloy design concepts and outcomes, *Adv. Eng. Mater.* 6 (2004) 299–303.
- [5] H. Diao, X. Xie, F. Sun, K.A. Dahmen, P.K. Liaw, Mechanical properties of high-entropy alloys, in: M.C. Gao, J.W. Yeh, P.K. Liaw, Y. Zhang (Eds.), *High-entropy Alloys: Fundamentals and Applications*, Springer International Publishing, Switzerland, 2016, pp. 181–236.
- [6] Y. Zhang, T.T. Zuo, Z. Tang, M.C. Gao, K.A. Dahmen, P.K. Liaw, Z.P. Lu, Microstructures and properties of high-entropy alloys, *Prog. Mater. Sci.* 61 (2014) 1–93.
- [7] Y. Zhang, Y.J. Zhou, J.P. Lin, G. Chen, P.K. Liaw, Solid-solution phase formation rules for multi-component alloys, *Adv. Eng. Mater.* 10 (2008) 534–538.
- [8] K.M. Youssef, A.J. Zaddach, C. Niu, D.L. Irving, C.C. Koch, A novel low-density, high-hardness, high-entropy alloy with close-packed single-phase nanocrystalline structures, *Mater. Res. Lett.* 2 (2014) 95–99.
- [9] Y.D. Wu, Y.H. Cai, X.H. Chen, T. Wang, J.J. Si, L. Wang, Y.D. Wang, X.D. Hui, Phase composition and solid solution strengthening effect in TiZrNbMoV high-entropy alloys, *Mater. Des.* 83 (2015) 651–660.
- [10] J.Y. He, H. Wang, H.L. Huang, X.D. Xu, M.W. Chen, Y. Wu, X.J. Liu, T.G. Nieh, K. An, Z.P. Lu, A precipitation-hardened high-entropy alloy with outstanding tensile properties, *Acta Mater.* 102 (2016) 187–196.
- [11] K. Ma, H. Wen, T. Hu, T.D. Topping, D. Isheim, D.N. Seidman, E.J. Lavermia, J.M. Schoenung, Mechanical behavior and strengthening mechanisms in ultrafine grain precipitation-strengthened aluminum alloy, *Acta Mater.* 62 (2014) 141–155.
- [12] W.H. Liu, Y. Wu, J.Y. He, T.G. Nieh, Z.P. Lu, Grain growth and the Hall-Petch relationship in a high entropy alloy FeCrNiCoMn, *Scripta Mater.* 68.7 (2013) 526–529.
- [13] Z. Li, K.G. Pradeep, Y. Deng, D. Raabe, C.C. Tasan, Metastable high-entropy dual-phase alloys overcome the strength-ductility trade-off, *Nature* 534 (2016) 227.
- [14] D. Raabe, C.C. Tasan, H. Springer, M. Bausch, From high-entropy alloys to high-entropy steels, *Steel Res. Int.* 86 (2015) 1127–1138.
- [15] B. Gludovatz, A. Hohenwarter, D. Catoor, E.H. Chang, E.P. George, R.O. Ritchie, A fracture-resistant high-entropy alloy for cryogenic applications, *Science* 345 (2014) 1153–1158.
- [16] B. Schuh, F. Mendez-Martin, B. Volker, E.P. George, H. Clemens, R. Pippan, A. Hohenwarter, Mechanical properties, microstructure and thermal stability of a nanocrystalline CoCrFeMnNi high-entropy alloy after severe plastic deformation, *Acta Mater.* 96 (2015) 258–268.
- [17] K.Y. Tsai, M.H. Tsai, J.W. Yeh, Sluggish diffusion in Co-Cr-Fe-Mn-Ni high-entropy alloys, *Acta Mater.* 61 (2013) 4887–4897.
- [18] L.R. Owen, E.J. Pickering, H.Y. Playford, H.J. Stone, M.G. Yucker, N.G. Jones, An assessment of the lattice strain in the CrMnFeCoNi high-entropy alloy, *Acta Mater.* 122 (2017) 11–18.
- [19] F. Otto, Y. Yang, H. Bei, E.P. George, Relative effects of enthalpy and entropy on the phase stability of equiatomic high-entropy alloys, *Acta Mater.* 61 (2013) 2628–2638.
- [20] B. Cantor, I.T.H. Chang, P. Knight, A.J.B. Vincent, Microstructural development in equiatomic multicomponent alloys, *Mater. Sci. Eng. A* 375–377 (2004) 213–218.
- [21] Z.J. Zhang, M.M. Mao, J. Wang, B. Gludovatz, Z. Zhang, S.X. Mao, E.P. George, Q. Yu, R.O. Ritchie, Nanoscale origins of the damage tolerance of the high-

- entropy alloy CrMnFeCoNi, *Nature Commun* 6 (2015) 10143.
- [22] O.N. Senkov, S.V. Senkova, C. Woodward, D.B. Miracle, Low-density, refractory multi-principal element alloys of the Cr–Nb–Ti–V–Zr system: microstructure and phase analysis, *Acta Mater.* 61 (2013) 1545–1557.
- [23] O.N. Senkov, C.F. Woodward, Microstructure and properties of a refractory NbCrMo<sub>0.5</sub>Ta<sub>0.5</sub>TiZr alloy, *Mater. Sci. Eng. A* 529 (2011) 311–320.
- [24] Y. Zou, S. Maiti, W. Steurer, R. Spolenak, Size-dependent plasticity in an Nb<sub>25</sub>Mo<sub>25</sub>Ta<sub>25</sub>W<sub>25</sub> refractory high-entropy alloy, *Acta Mater.* 65 (2014) 85–97.
- [25] É. Fazakas, V. Zadorozhnyy, L.K. Varga, A. Inoue, D.V. Louzguine-Luzgin, F.Y. Tian, L. Vitos, Experimental and theoretical study of Ti<sub>20</sub>Zr<sub>20</sub>Hf<sub>20</sub>Nb<sub>20</sub>X<sub>20</sub> (X=V or Cr) refractory high-entropy alloys, *Int. J. Refract. Met. Hard Mater* 47 (2014) 131–138.
- [26] B. Zhang, M.C. Gao, Y. Zhang, S.M. Guo, Senary refractory high-entropy alloy Cr<sub>x</sub>MoNbTaVW, *Calphad* 51 (2015) 193–201.
- [27] O.N. Senkov, D. Isheim, D.N. Seidman, A.L. Pilchak, Development of a refractory high entropy superalloy, *Entropy* 18 (2016) 102.
- [28] O.N. Senkov, S.V. Senkova, C. Woodward, Effect of aluminum on the microstructure and properties of two refractory high-entropy alloys, *Acta Mater.* 68 (2014) 214–228.
- [29] S. Singh, N. Wanderka, B.S. Murty, U. Glatzel, J. Banhart, Decomposition in multi-component AlCoCrCuFeNi high-entropy alloy, *Acta Mater.* 59 (2011) 182–190.
- [30] M.A. Hemphill, T. Yuan, G.Y. Wang, J.W. Yeh, C.W. Tsai, A. Chuang, P.K. Liaw, Fatigue behavior of Al<sub>0.5</sub>CoCrCuFeNi high entropy alloys, *Acta Mater.* 60 (2012) 5723–5734.
- [31] Y.P. Wang, B.S. Li, M.X. Ren, C. Yang, H.Z. Fu, Microstructure and compressive properties of AlCrFeCoNi high entropy alloy, *Mater. Sci. Eng. A* 491 (2008) 154–158.
- [32] Y.F. Kao, T.J. Chen, S.K. Chen, J.W. Yeh, Microstructure and mechanical property of as-cast, -homogenized, and -deformed Al<sub>x</sub>CoCrFeNi (0 < x < 2) high-entropy alloys, *J. Alloys Compd* 488 (2009) 57–64.
- [33] W.R. Wang, W.L. Wang, J.W. Yeh, Phases, microstructure and mechanical properties of Al<sub>x</sub>CoCrFeNi high-entropy alloys at elevated temperatures, *J. Alloys Compd* 589 (2014) 143–152.
- [34] T.T. Shun, Y.C. Du, Microstructure and tensile behaviors of FCC Al<sub>0.3</sub>CoCrFeNi high entropy alloy, *J. Alloys Compd* 479 (2009) 157–160.
- [35] Y. Ma, B.B. Jiang, C.L. Li, Q. Wang, C. Dong, P.K. Liaw, F. Xu, L. Sun, The BCC/B2 morphologies in Al<sub>x</sub>NiCoFeCr high-entropy alloys, *Metals* 7 (2017) 57.
- [36] Q. Wang, Y. Ma, B.B. Jiang, X. Li, Y. Shi, C. Dong, P.K. Liaw, A cuboidal B2 nanoprecipitation-enhanced body-centered-cubic alloy Al<sub>0.7</sub>CoCrFe<sub>2</sub>Ni with prominent tensile properties, *Scripta Mater.* 120 (2016) 85–89.
- [37] R.C. Reed, *The Superalloys: Fundamentals and Applications*, Cambridge University Press, New York, 2006.
- [38] X.G. Wang, J.L. Liu, T. Jin, X.F. Sun, The effects of ruthenium additions on tensile deformation mechanisms of single crystal superalloys at different temperatures, *Mater. Des.* 63 (2014) 286–293.
- [39] J. Sato, T. Omori, K. Oikawa, I. Ohnuma, R. Kainuma, K. Ishida, Cobalt-base high-temperature alloys, *Science* 312 (2006) 90–91.
- [40] W.W. Sun, R.K.W. Marceau, M.J. Styles, D. Barbier, C.R. Hutchinson, G phase precipitation and strengthening in ultra-high strength ferritic steels: towards lean 'maraging' metallurgy, *Acta Mater.* 130 (2017) 28–46.
- [41] S. Jiang, H. Wang, Y. Wu, X.J. Liu, H.H. Chen, M.J. Yao, B. Gault, D. Ponge, D. Raabe, A. Hirata, M.W. Chen, Y.D. Wang, Z.P. Lu, Ultrastrong steel via minimal lattice misfit and high-density nanoprecipitation, *Nature* 544 (2017) 460.
- [42] H.L. Hong, Q. Wang, C. Dong, P.K. Liaw, Understanding the Cu–Zn brass alloys using a short-range-order cluster model: significance of specific compositions of industrial alloys, *Sci. Rep.* 4 (2014), 7065–7065.
- [43] C. Pang, B.B. Jiang, Y. Shi, Q. Wang, C. Dong, Cluster-plus-glue-atom model and universal composition formulas [cluster](glue atom)<sub>x</sub> for BCC solid solution alloys, *J. Alloys Compd* 652 (2015) 63–69.
- [44] J.M. Cowley, Short- and long-range order parameters in disordered solid solutions, *Phys. Rev.* 120 (1960) 1648–1657.
- [45] J. Friedel, Electronic structure of primary solid solutions in metals, *Adv. Phys.* 50.6 (2001) 539–595.
- [46] W. Guo, W. Dmowski, J.Y. Noh, P. Rack, P.K. Liaw, T. Egami, Local atomic structure of a high-entropy alloy: an x-ray and neutron scattering study, *Metall. Mater. Trans. A* 44 (2013) 1994–1997.
- [47] M.C. Gao, D.E. Alman, Searching for next single-phase high-entropy alloy compositions, *Entropy* 15 (2013) 4504–4519.
- [48] L.J. Santodonato, Y. Zhang, M. Feyngenson, C.M. Parish, M.C. Gao, R.J. Weber, J.C. Neufeld, Z. Tang, P.K. Liaw, Deviation from high-entropy configurations in the atomic distributions of a multi-principal-element alloy, *Nature Commun* 6 (2015), 5964–5964.
- [49] Y. Ma, Q. Wang, C.L. Li, L.J. Santodonato, M. Feyngenson, C. Dong, P.K. Liaw, Chemical short-range orders and the induced structural transition in high-entropy alloys, *Scripta Mater.* 144 (2018) 64–68.
- [50] A. Takeuchi, A. Inoue, Calculations of mixing enthalpy and mismatch entropy for ternary amorphous alloys, *Mater. Trans.* 41 (2000) 1372–1378.
- [51] D.B. Cullity, S.R. Stock, *Elements of X-Ray Diffraction*, Prentice Hall, New Jersey, America, 2011.
- [52] W.F. Hosford, *Mechanical Behavior of Materials*, first ed., Cambridge University Press, New York, America, 2005.
- [53] K.H. Lo, C.H. Shek, J.K.L. Lai, Recent developments in stainless steels, *Mater. Sci. Eng. R* 65 (2009) 39–104.
- [54] T. Egami, Y. Waseda, Atomic size effect on the formability of metallic glasses, *J. Non-Cryst. Solids* 64 (1984) 113–134.
- [55] X. Yang, Y. Zhang, Prediction of high-entropy stabilized solid-solution in multi-component alloys, *Mater. Chem. Phys.* 132 (2012) 233–238.
- [56] C.L. Gan, G.L. Chen, Y. Zhang, Phase change and mechanical behaviors of Ti<sub>x</sub>CoCrFeNiCu<sub>1-y</sub>Al<sub>y</sub> high entropy alloys, *J. ASTM Int* 7 (2010) 1–8.
- [57] J.Y. He, W.H. Liu, H. Wang, Y. Wu, X.J. Liu, T.G. Nieh, Z.P. Lu, Effects of Al addition on structural evolution and tensile properties of the FeCoNiCrMn high-entropy alloy system, *Acta Mater.* 62 (2014) 105–113.
- [58] C. Kittel, J.F. Masi, Introduction to solid state physics, *Am. J. Phys.* 21 (1996) 547–548.
- [59] S. Guo, C. Ng, J. Lu, C.T. Liu, Effect of valence electron concentration on stability of fcc or bcc phase in high entropy alloys, *J. Appl. Phys.* 109 (2011) 645–647.
- [60] O.N. Senkov, C. Woodward, D.B. Miracle, Microstructure and properties of aluminum-containing refractory high-entropy alloys, *JOM* 66 (2014) 2030–2042.
- [61] P.W. Voorhees, G.B. Mcfadden, W.C. Johnson, On the morphological development of second-phase particles in elastically-stressed solids, *Acta Metall. Mater.* 40 (1992) 2979–2992.
- [62] P. Fratzl, O. Penrose, J.L. Lebowitz, Modeling of phase separation in alloys with coherent elastic misfit, *J. Stat. Phys.* 95 (1999) 1429–1503.
- [63] M.E. Thompson, C.S. Su, P.W. Voorhees, The equilibrium shape of a misfitting precipitate, *Acta Metall. Mater.* 42 (1994) 2107–2122.
- [64] E.A. Marquis, D.N. Seidman, Nanoscale structural evolution of Al<sub>3</sub>Sc precipitates in Al(Sc) alloys, *Acta Mater.* 49 (2001) 1909–1919.
- [65] R.J. Wasilewski, Elastic constants and young's modulus of NiAl, *Trans. Mct. Soc. AIME* 236 (1996) 455.
- [66] T. Hong, A.J. Freeman, Effect of antiphase boundaries on the electronic structure and bonding character of intermetallic systems: NiAl, *Phys. Rev. B: Condensed Matter* 43 (1991) 6446–6458.
- [67] R. Kikuchi, J.W. Cahn, Theory of interphase and antiphase boundaries in F.C.C. alloy, *Acta Metall.* 27 (1979) 1337–1353.
- [68] A.J. Ardell, Precipitation hardening, *Metall Trans A* 16A (1985) 1985–2135.
- [69] A. Argon, *Strengthening Mechanisms in Crystal Plasticity*, Oxford University Press, Oxford, the United Kingdom, 2007.
- [70] V. Gerold, H. Haberkorn, On the critical resolved shear stress of solid solutions containing coherent precipitates, *Phys. Stat. Sol* 16 (1966) 675–684.
- [71] B. Jansson, A. Melander, On the critical resolved shear stress from misfitting particles, *Scripta Metall.* 12 (1978) 497–498.
- [72] A. Melander, P.A. Persson, The strength of a precipitation hardened AlZnMg alloy, *Acta Metall.* 26 (1978) 267–278.
- [73] E. Nembach, Precipitation hardening caused by a difference in shear modulus between particle and matrix, *Phys. Stat. Sol* 78 (1983) 571–581.
- [74] H. Gleiter, E. Hornbogen, Theorie der Wechselwirkung von Versetzungen mit kohärenten geordneten Zonen, *Phys. Stat. Sol* 12 (1965) 235–250.
- [75] ASM International Handbook committee, *Properties and Selection: Irons, Steels and High Performance Alloys*, second ed., vol. 1, ASM International, America, 1993.
- [76] E. Orowan, in: *Symposium on Internal Stress in Metals and Alloys*, Institute of Metals, London, 1948, pp. 451–453.
- [77] L.M. Brown, R.K. Ham, Dislocation-particle interactions, in: A. Kelly, R.B. Nicholson (Eds.), *Strengthening Methods in Crystals*, Elsevier, Amsterdam, 1971, pp. 9–135.
- [78] E. Nembach, Particle strengthening of metals and alloys, *Mater. Sci. Technol.* 3 (1997) 329–337.
- [79] A.S. Argon, T.M. Pollock, Creep resistance of CMSX-3 nickel base superalloy single crystals, *Acta Mater.* 40 (1992) 1–30.